



# Effect of trace carbon on the dynamic compressive properties in the as-cast Ti13V11Cr3Al alloy

Duoduo Wang<sup>a,b,c</sup>, Qunbo Fan<sup>a,b,c,\*</sup>, Haichao Gong<sup>a,b</sup>, Xinjie Zhu<sup>a,b</sup>

<sup>a</sup> School of Materials Science and Engineering, Beijing Institute of Technology, Beijing, 100081, China

<sup>b</sup> National Key Laboratory of Science and Technology on Materials Under Shock and Impact, Beijing, 100081, China

<sup>c</sup> Beijing Institute of Technology Chongqing Innovation Center, Chongqing, 401135, China

## ARTICLE INFO

### Keywords:

Titanium alloy  
Carbon  
TiC  
Diagram  
Dynamic compressive properties  
Adiabatic shear bands

## ABSTRACT

An as-cast Ti13V11Cr3Al titanium alloy was fabricated via vacuum induction skull melting. The microstructure and mechanical properties of this alloy were characterized via transmission electron microscopy (TEM) combined with energy-dispersive X-ray spectroscopy (EDX) and compression experiments, respectively. The results revealed that trace impurity carbon (0.014 wt%) led to the formation of in-situ needle-like TiC precipitates during solidification. To reveal the underlying mechanism governing this formation, the (Ti13V11Cr3Al)-C pseudo-phase equilibrium diagram was constructed using JMatPro software. The results suggested that the precipitation of TiC will occur if the carbon content is > 0.003 wt%. Under high strain rate conditions, small volume fractions of these precipitates can lead to improvements in the ductility, and retention of the strength (1350 MPa). The as-cast alloy exhibited excellent dynamic plasticity, as evidenced by a critical fracture strain of >35% at a strain rate of 4158/s. In addition, microstructural observation of adiabatic shear bands revealed that debonding of the TiC precipitates from the matrix required considerable energy dissipation. Moreover, a crack propagated along the boundary of the precipitates, thereby leading to significant improvement in the dynamic plasticity from the other respect.

## 1. Introduction

Titanium alloys are characterized by excellent properties, such as low density, high specific strength, good toughness, and corrosion resistance [1–3], and are therefore used extensively in aerospace, armor protection, and other service environments. The service performance of titanium alloys is strongly dependent on the microstructures comprising these materials [4,5]. Therefore, the differences in microstructures caused by impurity elements (such as trace carbon) will have a significant effect on this performance [6]. However, studies considering the effect of trace carbon on the micro-morphology of titanium alloys have rarely been reported. Zhao et al. [7,8] fabricated Ti-xNb  $\beta$ -titanium alloy via metal injection molding. The carbon content, originating from trace impurities in titanium and niobium powders, of the as-sintered samples was only 0.06 wt%. Furthermore, the precipitation of TiC<sub>x</sub> at grain boundaries was characterized. Kafkas et al. [9] determined the microstructural characteristics of a Ti-24Nb-4Zr-8Sn alloy also fabricated via metal injection molding. To reveal the precipitation mechanism of TiC<sub>x</sub> thermodynamically, Zhao et al. [10] constructed (Ti-16Nb)-C and Ti-C

pseudo-binary phase diagrams using Thermo-Calc software. Comparative analysis indicated that the solubility limit of carbon in  $\beta$ -Ti was 0.12 wt% for the Ti-C alloy, and considerably lower (i.e., only 0.036 wt%) for the Ti-16Nb alloy. Yan et al. [11] investigated the mechanism governing TiC<sub>x</sub> precipitation in Ti-15Mo titanium alloy. The aforementioned results indicated that the solubility limit of carbon in  $\beta$ -Ti varied significantly with alloy composition, and values as low as 0.006 wt% were obtained for special titanium alloys [7,10]. The precipitation of in-situ TiC<sub>x</sub> will occur once the content of trace carbon exceeds the solubility limit of carbon in  $\beta$ -Ti.

TiC<sub>x</sub> precipitates exhibit high hardness, good thermal stability, and good compatibility with titanium. Furthermore, these precipitates can act as heterogeneous nuclei that retard dislocation movement, thereby leading to significant improvement in the strength of titanium alloys. Nevertheless, as a brittle phase, TiC<sub>x</sub> can also lead to reductions in the ductility of these alloys, as confirmed by Zhao [10] and Du [12] via quasi-static tensile tests. The compression experiments of titanium matrix composites also exhibited similar mechanical response behavior [13–17]. However, other studies have reported that TiC<sub>x</sub> has a positive

\* Corresponding author. School of Materials Science and Engineering, Beijing Institute of Technology, Beijing, 100081, China.

E-mail address: [fanqunbo@bit.edu.cn](mailto:fanqunbo@bit.edu.cn) (Q. Fan).

<https://doi.org/10.1016/j.intermet.2020.106818>

Received 8 October 2019; Received in revised form 1 April 2020; Accepted 26 April 2020

Available online 7 May 2020

0966-9795/© 2020 Elsevier Ltd. All rights reserved.

effect on the ductility of titanium alloys [18–21]. Mereddy et al. [18] found that the formation of in-situ TiC could lead to significant grain size refinement. Correspondingly, the post-fracture elongation of the Ti6Al4V0.1C (~14.5%) was higher than that of the Ti6Al4V0.41 alloy (~1%). Li et al. [21] used a wavelength-dispersive X-ray spectroscopy (WDXS) technique to investigate the effects of carbon on the microstructures and mechanical properties of a Ti-25 V-15Cr-2Al alloy. The results indicated that in-situ TiC<sub>x</sub> exhibited strong oxygen absorption capacity, and thus improved the overall tensile ductility of the alloy by reducing the oxygen content of the Ti matrix [19,20].

The effect of in-situ TiC<sub>x</sub> on the ductility of titanium alloys under quasi-static loading conditions has been extensively investigated. However, in order to broaden the application range of these alloys, many extreme conditions, such as high strain-rates and shock loading, should be carefully considered. A few researchers have explored the effect of TiC<sub>x</sub> on the dynamic compressive properties of titanium matrix composites at room temperature. For example, using carbon fibers as a carbon source, Hao et al. [22] found that the dynamic compressive strength of TiC/Ti6Al4V composites can be improved significantly under the premise of maintaining good plasticity. This improvement was attributed to the formation of in-situ TiC. Microcracks were initiated in the material and propagated around the hard TiC precipitates, ultimately leading to shear failure of the material. However, the influence of trace in-situ TiC on the dynamic plasticity of titanium alloys has insufficient investigation. Furthermore, scarcely works about the mechanism governing this influence have been conducted. Therefore, in this work, Ti13V11Cr3Al titanium alloy containing 0.014 wt% carbon was fabricated via vacuum induction skull melting. The microstructural and the mechanical properties of the alloy were investigated. Moreover, from the aspect of adiabatic shear bands (ASB), the inherent mechanism governing the effect of trace in-situ TiC on the improvement of dynamic plasticity was further analyzed.

## 2. Material and methods

The chemical composition of the raw materials used for the  $\beta$  titanium alloy Ti13V11Cr3Al ingot investigated in this work is shown in Table 1. The vanadium, chromium, and aluminum elements in the alloy were added in the form of an Al80 V master alloy, a chromium powder, and an aluminum shot, respectively. Theoretical calculations showed that the sponge titanium and the Al80 V master alloy introduced 0.014 wt% impurity carbon. The alloy was prepared at China Iron & Steel Research Institute (CISRI) using a vacuum induction skull melting furnace with a water-cooling copper crucible (VISM-20, Beijing, China). To fabricate the Ti13V11Cr3Al ingot, the raw materials were proportioned and thoroughly blended in compacts. These mixture compacts and the sponge titanium were subsequently compressed into electrodes. Afterward, the electrodes were melted repeatedly (three times) by means of induction heating and the melt was then poured into a graphite mold. After the procedure was completed, a 20 kg (weight) 290 mm  $\times$  80 mm  $\times$  110 mm (size) ingot was obtained. Furthermore, the ingot was heat-treated at 780 °C for 1 h, and then air cooled (denoted as heat-treated alloy).

The microstructure and the ASB morphology of the Ti13V11Cr3Al titanium alloy were characterized via Optical Microscopy (OM; LECO series Olympus PME-3) and Scanning Electron Microscopy (SEM;

Japanese Hitachi S-4800 N). Prior to this characterization, the specimens were ground with various grades (120# to 1500#) of sandpaper. The surfaces of the specimens were then polished via the synergistic effect of lapping paste Fe<sub>2</sub>O<sub>3</sub> and polishing agent Cr<sub>2</sub>O<sub>3</sub>. Subsequently, the polished specimens were chemically etched in a premixed corrosive solution (2 vol% HF, 10 vol% HNO<sub>3</sub>, and 88 vol% H<sub>2</sub>O). Afterward, transmission electron microscopy (TEM; Tencai G20FEI field emission high-resolution TEM) bright field (BF) images of the as-cast specimens were obtained. Small discs (diameter: 3 mm) were then prepared using a wire cutting machine, and mechanically polished to a thickness of ~100  $\mu$ m. These discs were then electrolytically polished (volume ratio of electrolyte solution: HClO<sub>4</sub>:CH<sub>3</sub>(CH<sub>2</sub>)<sub>3</sub>OH:CH<sub>3</sub>OH = 6:34:60, accelerating voltage: 30 V, temperature: -40 °C. Furthermore, the crystal structures of the precipitates were determined via X-ray diffraction (XRD).

The dynamic compression experiments at room temperature were performed on  $\Phi 5 \times 5$  mm specimens by using a Split Hopkinson Pressure Bar system (SHPB, BIT, China). Furthermore, for the as-cast Ti13V11Cr3Al titanium alloy, the complex microstructural evolution of the ASB was investigated.

## 3. Results and discussion

Fig. 1 shows the microstructural morphology of the Ti13V11Cr3Al titanium alloy. The average grain sizes of the as-cast and heat-treated alloys remain essentially the same (i.e., ~700–800  $\mu$ m), as shown in Fig. 1(a) and (d). Trace in-situ spherical precipitates (size: 3–4  $\mu$ m) are uniformly distributed inside the grains in the as-cast alloy, whereas inhomogeneous distribution occurs for the heat-treated alloy (see Fig. 1 (b) and (e), respectively). Furthermore, the grains of the heat-treated alloy are divided into smaller structures by relatively more precipitates than the as-cast alloy. The precipitates accumulate along the grain boundaries before and after the heat treatment, exhibiting a necklace shape. Fig. 1(c) shows a magnified view of the region enclosed in the red circle (see Fig. 1(b)). The dispersive distribution of relatively fine nanoscale precipitates is observed.

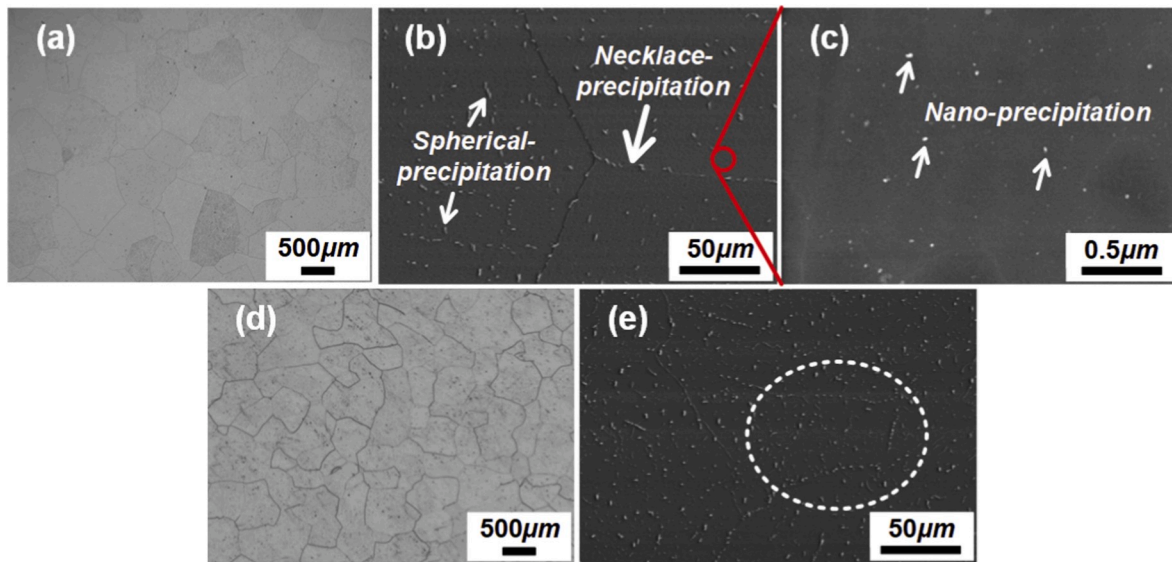
Fig. 2 shows the XRD patterns of the Ti13V11Cr3Al titanium alloy. For the as-cast alloy (see red line in Fig. 2), the prominent diffraction peaks ( $2\theta = 39^\circ, 57^\circ, \text{ and } 72^\circ$ ) correspond to a  $\beta$ -Ti phase with a body-centered-cubic structure. For the heat-treated alloy (see blue line in Fig. 2), a new diffraction peak ( $2\theta = 36^\circ$ ) is detected except for the typical reflections of  $\beta$ -Ti phase in as-cast alloy. This comparative analysis suggests that the precipitates in the heat-treated alloy may be pronounced, consistent with the results shown in Fig. 1 (e). Furthermore, the measured interplanar spacing of the new reflection (2.486 Å) is relatively close to the value obtained for the (111)TiC reflection (2.493 Å) and, hence, precipitates can be preferentially determined to be TiC.

Fig. 3 shows the TEM-BF images and TEM-EDX results of the as-cast Ti13V11Cr3Al titanium alloy. The TEM-BF images of the  $\beta$ -Ti matrix and TiC precipitate are shown in Fig. 3(a) and (b), respectively. The selected area electron diffraction (SAED) pattern (Fig. 3(a) inset) confirms the body-centered-cubic structure of the  $\beta$ -Ti matrix. Compared with the SEM image in Fig. 1, Fig. 3(b) reveals more detailed morphology, i.e., needle-like precipitates with aspect ratio  $\gg 1$ . The chemical composition of the precipitates is determined via TEM-EDX analysis of two typical

Table 1

Chemical composition of the raw materials used for the  $\beta$  titanium alloy Ti13V11Cr3Al ingot.

Element (wt.%)	O	Fe	Si	C	V	Al	Cr	Weight (kg)
Sponge titanium	0.038	0.01	0.01	0.008	—	—	—	14.579
Al80V	0.15	0.15	0.19	0.05	83.5	15.96	—	3.114
Aluminum shot	—	0.12	0.03	—	—	99.7	—	0.103
Chromium powder	0.06	0.13	0.11	—	—	—	99.82	2.204
Electrodes	0.058	0.046	0.049	0.014	13	3	11	20



**Fig. 1.** Microstructural morphology of the Ti13V11Cr3Al titanium alloy: (a) OM image at a magnification of  $25\times$ , as-cast, (b) SEM image at a magnification of  $500\times$ , as-cast, (c) SEM image at a high-magnification ( $50k\times$ ) of region enclosed in the red circle shown in (b), (d) OM image at a magnification of  $25\times$ , heat-treated, (e) SEM image at a magnification of  $500\times$ , heat-treated.

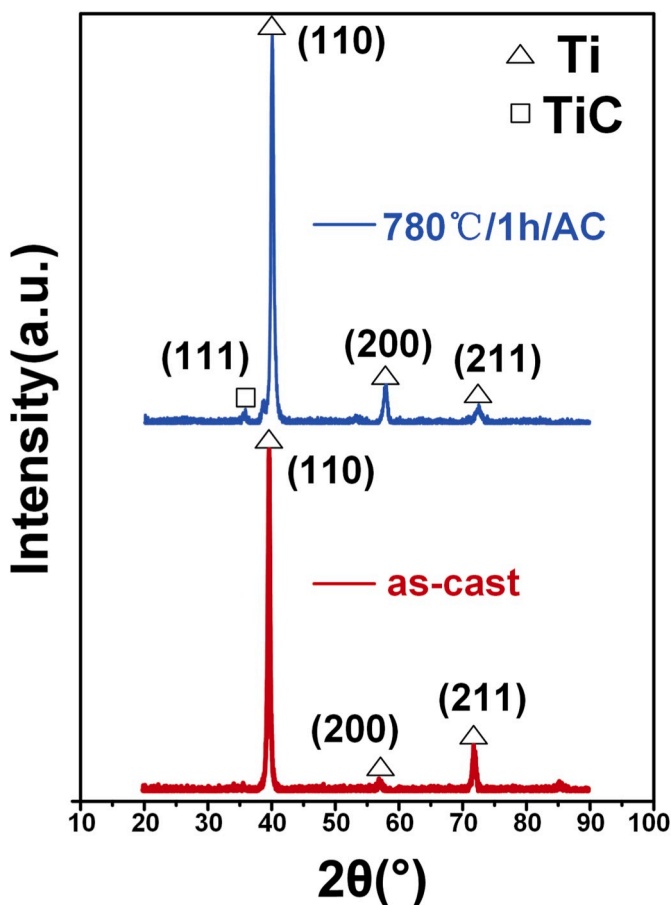


**Fig. 2.** XRD patterns of the Ti13V11Cr3Al titanium alloy.

positions (Fig. 3(b)) shown in Fig. 3 (c) and (d), respectively. Comparative analysis indicates that the C/Ti atom ratio at position 1 (denoted as the precipitate) is  $\sim 1$ , whereas a rather low C/Ti atom ratio occurs at position 2 (denoted as the  $\beta$ -Ti matrix). Therefore, based on the effect of inevitable deviation, the precipitate is determined to be TiC produced by

trace carbon [12,18]. The electron diffraction spots shown in the inset of Fig. 3(b) can further confirm the existence of the face-centered-cubic TiC phase (JCPDS 659622). Furthermore, a small amount of twin structure (indicated by blue lines in Fig. 3(b) inset) forms during the nucleation and growth of TiC, as reported in previous studies [23–25].

To reveal the underlying precipitation mechanism of TiC, the pseudo-phase equilibrium diagrams for (Ti13V11Cr3Al)-C is constructed using CALPHAD model of JMatPro software, as illustrated in Fig. 4. The vanadium, chromium, and aluminum contents are constant at 13 wt%, 11 wt%, and 3 wt%, respectively, whereas the carbon content increases up to 0.3 wt%. Considering that the ingot is fabricated at a temperature of  $\sim 1600^\circ\text{C}$  and the diffusion of carbon atoms is virtually suppressed at relatively low temperatures, the calculated temperature ranges from  $400^\circ\text{C}$  to  $1600^\circ\text{C}$ . As shown in Fig. 4(a), during subsequent cooling from a high temperature of  $1600^\circ\text{C}$ , the  $\beta$ -Ti solidifies preferentially from the molten liquid and subsequently, TiC starts to precipitate in the molten metal  $\beta$ -Ti. The solubility of carbon decreases monotonically with decreasing temperature, indicating that the amount of TiC precipitating from the matrix increases. Afterward, the  $\beta$ -Ti  $\rightarrow$   $\alpha$ -Ti formation temperature ( $\sim 715^\circ\text{C}$ ) is reached, and thus  $\alpha$ -Ti is formed. In contrast, when the temperature decreases to values lower than the  $\alpha$ -Ti formation temperature, the solubility of carbon increases and then decreases. The minimum solubility of carbon in  $\beta$ -Ti is determined by examining the region enclosed in the circle shown in Fig. 4(a). This examination reveals a critical carbon level of  $\sim 0.003$  wt%. The TiC will form when the carbon content of the Ti13V11Cr3Al titanium alloy exceeds this value, i.e., TiC is extremely sensitive to trace carbon. In addition, although the formation of  $\alpha$ -Ti is described in the equilibrium phase diagram, the rapid cooling rate prevents this formation during solidification (see Figs. 1 and 2).

Considering the non-equilibrium cooling conditions, Fig. 5 shows the simulation results of the Ti13V11Cr3Al titanium alloy based on the Scheil-Gulliver model. As illustrated in Fig. 5(a), the  $\beta$ -Ti solidifies preferentially from the molten liquid during the melting process. Afterward, TiC precipitates are formed (albeit with low content) when the temperature is gradually decreased to values below  $1415^\circ\text{C}$ . To further investigate the formation of these precipitates, an abnormal evolution region of the orange line shown in Fig. 5(a) is closely examined (see Fig. 5(b)). As the temperature decreases from  $885^\circ\text{C}$  to  $723^\circ\text{C}$ , the TiC content increases monotonically to a maximum value of 0.075 wt%. The content decreases to 0.009 wt% with further reduction in temperature,

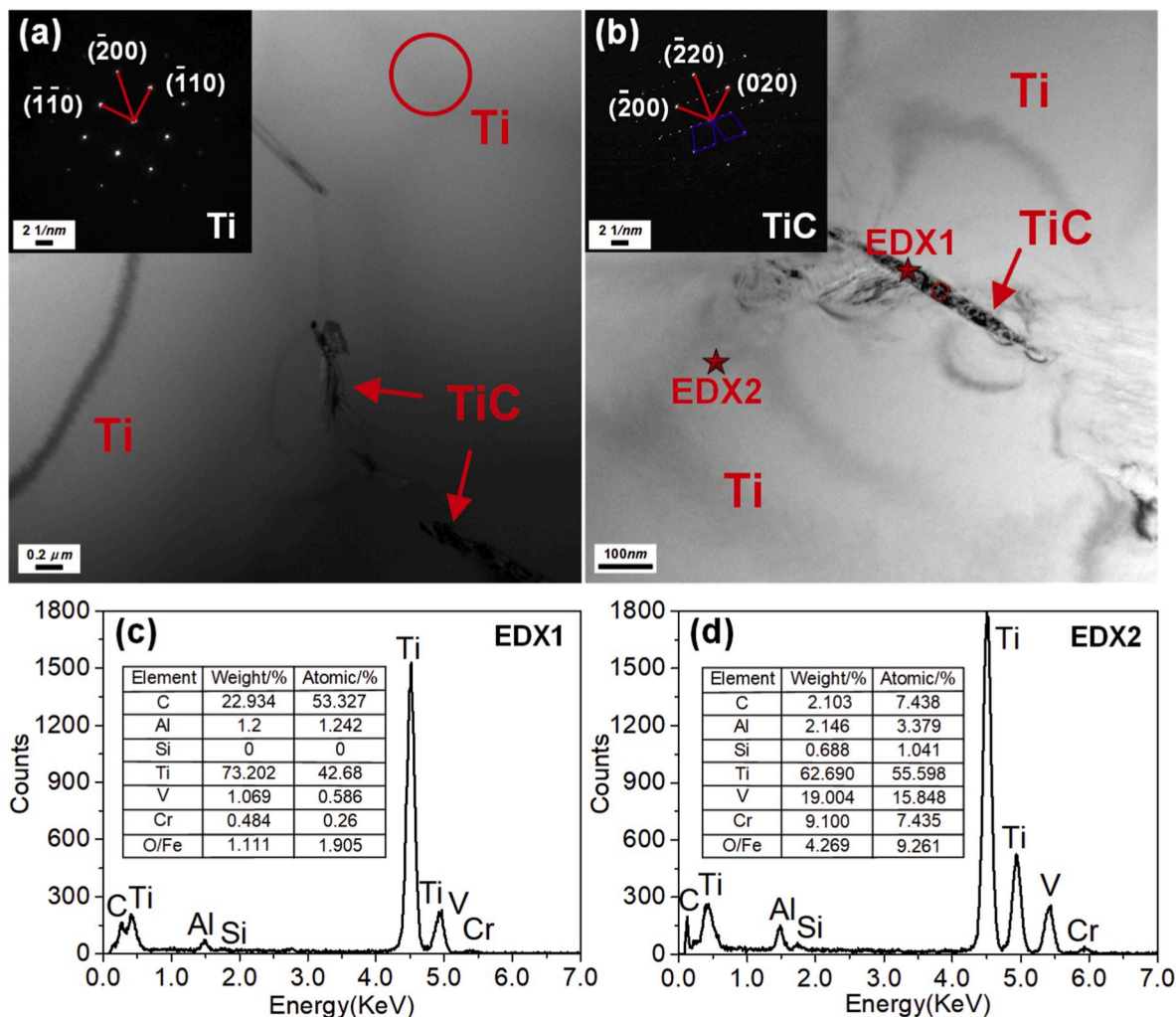


Fig. 3. TEM-BF images and TEM-EDX results of the as-cast Ti13V11Cr3Al titanium alloy: (a) and (b) are TEM-BF images of the  $\beta$ -Ti matrix and TiC precipitate, the corresponding SAED patterns are shown in the insets, (c) and (d) show the TEM-EDX results obtained from two typical positions shown in (b).

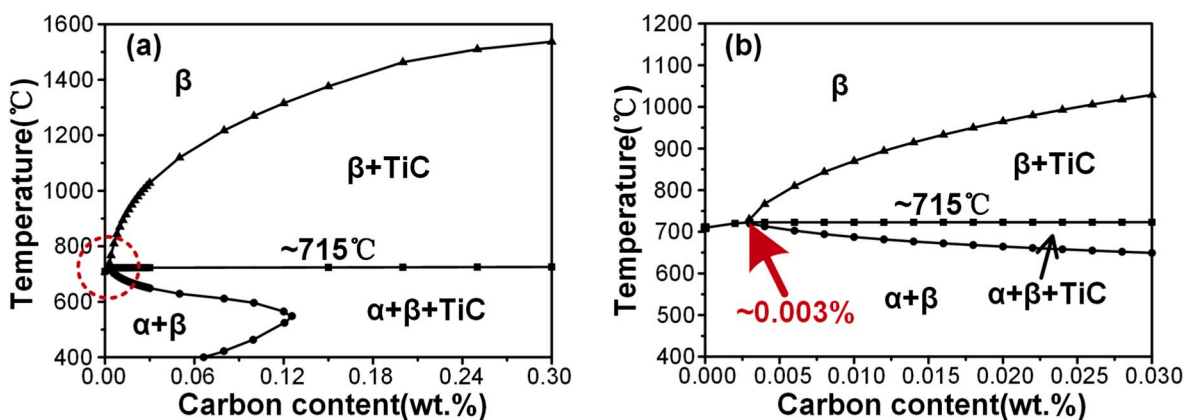


Fig. 4. Pseudo-phase equilibrium diagrams for (Ti13V11Cr3Al)-C, constructed using CALPHAD model of JMatPro software: (a) up to 0.30 wt% C, (b) up to 0.030 wt% C, magnified view of the region enclosed in the circle shown in (a).

which may be caused by a sudden increase in the solubility of carbon. This is consistent with the overall trend describing the solubility of carbon, as illustrated in Fig. 4. Furthermore, compared with other temperature conditions, the content of TiC in the heat-treated alloy ( $T_H = 780\text{ }^\circ\text{C}$ ) is at a relatively higher level (i.e.,  $\sim 0.06\text{ wt}\%$ ). This is consistent with the results that the heat-treated alloy exhibits more

pronounced precipitates than the as-cast alloy (see Fig. 1).

The phase transformations between titanium and titanium carbide are proceeded primarily by the diffusion of carbon atoms. The schematic in Fig. 6 shows the diffusion mechanism of carbon atoms during the solidification process of the as-cast Ti13V11Cr3Al titanium alloy. As Fig. 6(a) shows, during the solidification of the  $\beta$ -Ti, the carbon atoms

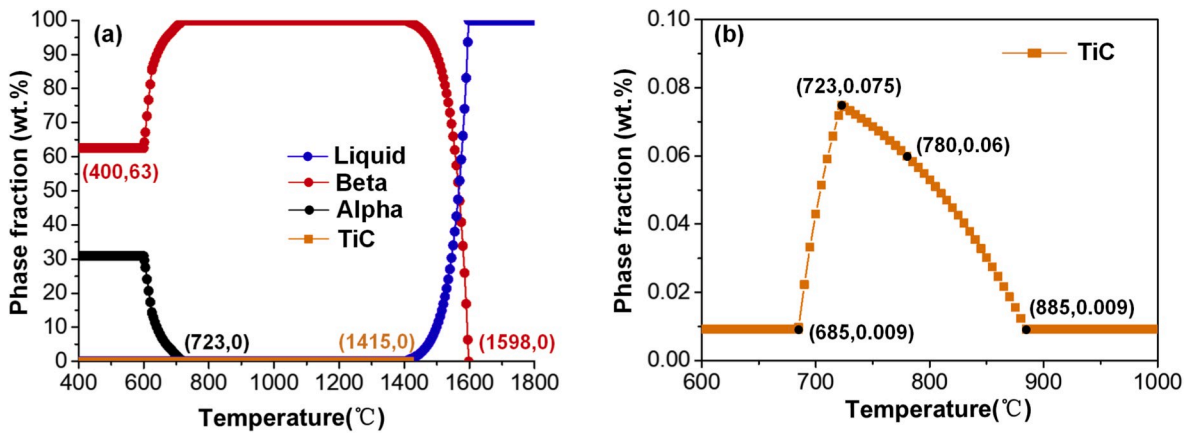


Fig. 5. Non-equilibrium solidification behavior of the Ti13V11Cr3Al titanium alloy, constructed using Scheil-Gulliver model of JMatPro software [26,27]: (a) each phase, (b) TiC precipitate, magnified view of an abnormal evolution region of the orange line in (a).

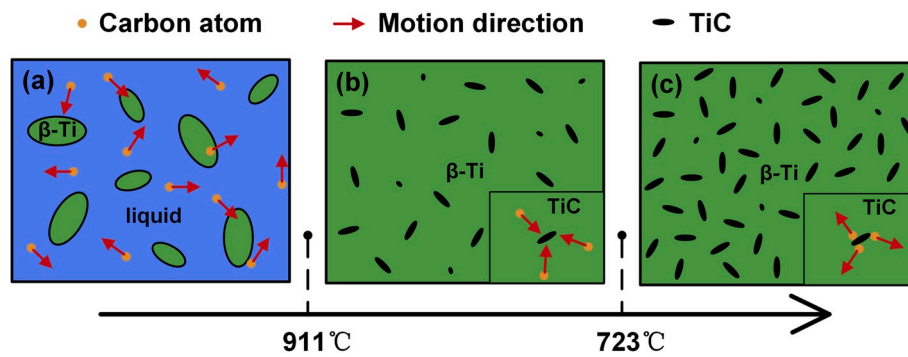


Fig. 6. Schematic of carbon atoms diffusion mechanism operating during the solidification process of the as-cast Ti13V11Cr3Al titanium alloy.

move irregularly throughout the molten liquid. When the temperature is gradually decreased to lower than 1415 °C, the atoms accumulate in local regions of the  $\beta$ -Ti, as shown in Fig. 6(b). The carbon content of these local carbon-rich areas may reach or exceed the critical carbon level of  $\beta$ -Ti (0.003 wt%), thereby leading to the formation of TiC. Furthermore, the movement of carbon atoms contributes to a further increase in the TiC content of the entire material, with the maximum content occurring at 723 °C. However, the solubility of carbon increases suddenly when the temperature decreases further (Fig. 4(a)) and, hence, the amount of carbon atoms diffusion in the local carbon-rich areas decreases. This is detrimental to the accumulation of TiC, as illustrated in Fig. 6(c).

Fig. 7 shows the true stress-logarithmic strain curves of the Ti13V11Cr3Al titanium alloy at room temperature. As shown in Fig. 7 (a), similar experimental results are obtained for the three samples subjected to quasi-static tensile load conditions. The ultimate tensile

strength (UTS) and ultimate elongation (UE) of 860 MPa and 10.4%–12.2%, respectively, are estimated for the as-cast alloy. In addition, considering the strain rate effect, the dynamic compression tests of the as-cast alloy are conducted at various strain rates, as illustrated in Fig. 7 (b). At high strain rates, the true stress increases monotonically with increasing the logarithmic strain in the elastic deformation stage. Subsequently, the true stress starts to decrease slightly after reaching the peak value, which is different from the quasi-static loading (see Fig. 7 (a)). Such softening behavior results from the low thermal conductivity of titanium alloy. During the dynamic compression, the adiabatic heating transformed by the plastic deformation is difficult to diffuse away. This causes that the thermal softening induced by dislocation annihilation counteracts to the strain hardening induced by dislocation multiplication [28–30]. In addition, the results suggest that the dynamic compressive strengths of the as-cast alloy remain approximately the same (i.e., 1350 MPa at 3445/s–4158/s). This is attributed to the

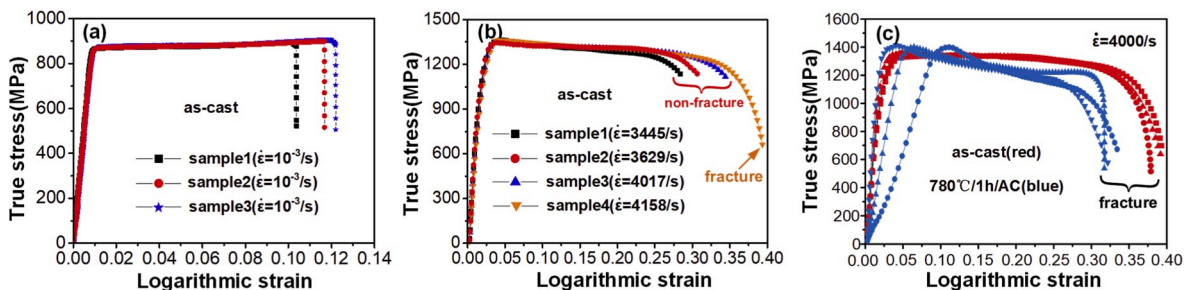
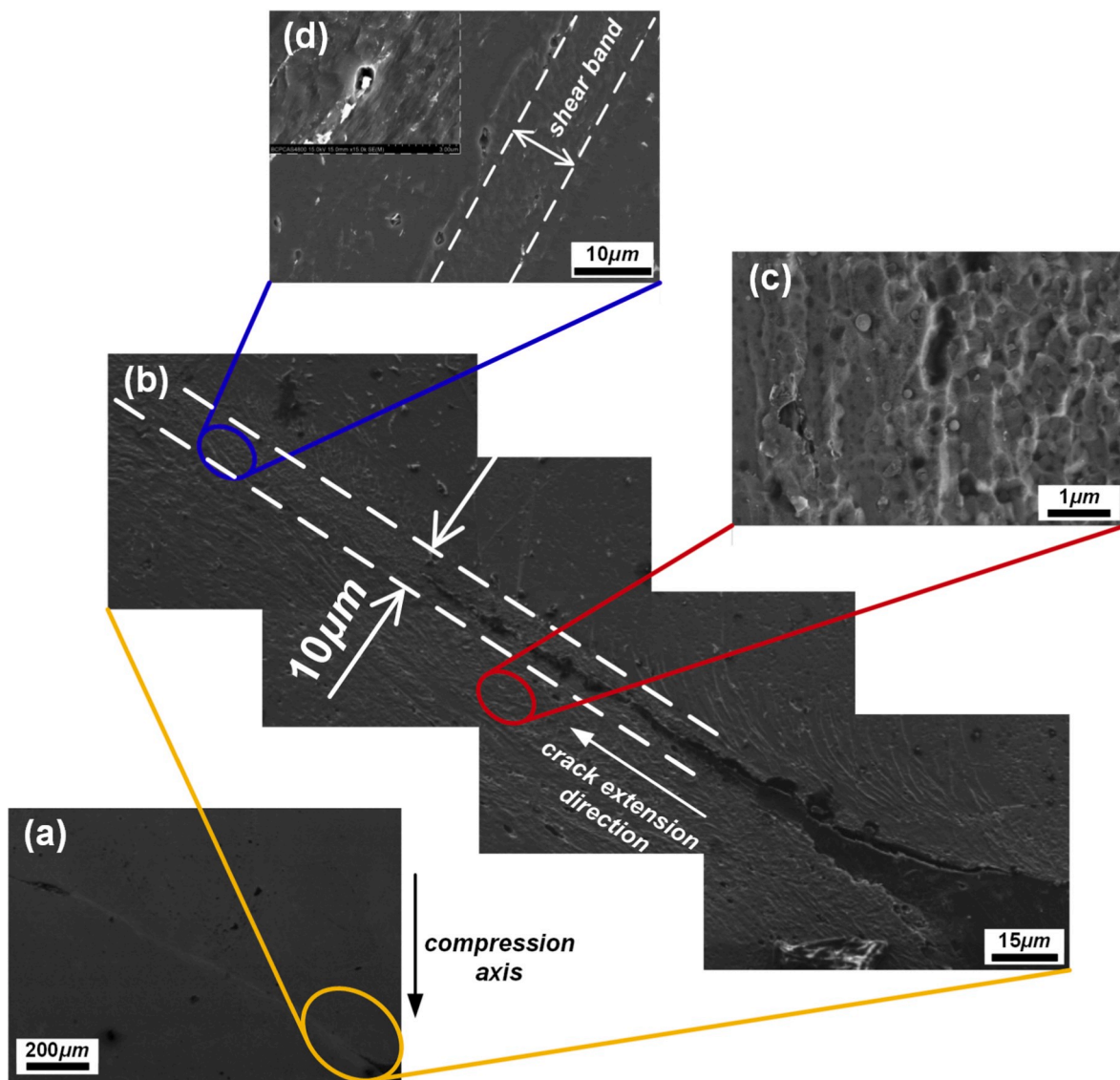


Fig. 7. True stress-logarithmic strain curves of the Ti13V11Cr3Al titanium alloy at room temperature: (a) quasi-static tensile, as-cast, (b) dynamic compression at various strain rates, as-cast, (c) dynamic compression of the as-cast (red) and heat-treated (blue) alloys at a strain rate of 4000/s.

dynamic equilibrium between the strain rate hardening and the thermal softening behavior [31]. Catastrophic fracture failure occurs only when the strain rate is further increased to 4158/s, i.e., the critical fracture strain of the as-cast alloy is extremely sensitive to strain rates and can be determined to be  $>35\%$  at 4158/s. Compared with other titanium alloys reported in previous studies [32–34], the as-cast Ti13V11Cr3Al alloy exhibits excellent dynamic plasticity. Furthermore, Fig. 7(c) shows the dynamic compression properties of the as-cast (red) and heat-treated (blue) alloys at a strain rate of 4000/s. Both alloys exhibit a relatively close dynamic compressive strength ( $\sim 1350$  MPa). The dynamic ductility of the as-cast alloy ( $\sim 0.35$ ) is significantly greater than that of the heat-treated alloy ( $\sim 0.3$ ). According to the microstructural characterization in Fig. 1, it can be inferred that the excellent dynamic plasticity of the as-cast alloy is related to the trace TiC.

ASB is considered a precursor for titanium alloy failure under high strain rates. To validate the deduction that in-situ trace TiC is beneficial to improve dynamic plasticity, the stop rings are used to control strains for the as-cast Ti13V11Cr3Al titanium alloy under dynamic compression loading. An ASB-containing sample (representing the onset of failure) at a strain of  $\epsilon = 31\%$  is obtained. Fig. 8(a) shows that the main crack is initiated and then propagates along a  $45^\circ$  shear direction. ASBs are

observed in the areas where the crack coalescence is insufficient, showing a white-etching band. Fig. 8(b) shows a high-magnification image of the region enclosed in the yellow ellipse (see Fig. 8(a)). A width of  $\sim 10 \mu\text{m}$  is determined for the ASB. Fig. 8(c) shows a high-magnification image of the region enclosed in the red ellipse (see Fig. 8(b)). The interface debonding behavior occurs between nanoprecipitates and matrix, thereby resulting in microscopic grooves in the ASB. This indicates that the TiC precipitates will be pulled out from the matrix by overcoming the friction resistance of the interface. Therefore, considerable energy dissipation is required before the rapid propagation of the main crack, thereby suppressing premature failure and improving the dynamic plasticity of the as-cast Ti13V11Cr3Al titanium alloy. Furthermore, the microstructure comprising the crack tip is revealed by a magnified view (see Fig. 8(d)) of the region enclosed in the blue ellipse (see Fig. 8(b)). The crack will deviate from the original direction and propagate along the boundary of the TiC precipitate. After bypassing the precipitate, the crack continues to propagate along the  $45^\circ$  direction. Therefore, the propagation path of the crack increases and, hence, the dynamic plasticity will be improved. It is plausible to speculate that the main crack will pass straight through the matrix in an alloy without TiC precipitates, i.e., the dynamic plasticity of this alloy is lower



**Fig. 8.** Microstructural evolution of the ASB: SEM image obtained at a magnification of (a)  $100\times$ , (b)  $1500\times$ , presenting a magnified view of the region enclosed in the yellow ellipse shown in (a), (c) and (d)  $20k\times$ , presenting a magnified view of the regions enclosed in the red and blue ellipses, respectively, shown in (b).

than the as-cast Ti13V11Cr3Al titanium alloy. In addition, it might be noted that brittle TiC precipitate will become a premature failure position if the content is further increased. The stress concentration could occur inevitably owing to the poor deformation compatibility between TiC and matrix [13,14]. This can qualitatively explain that the dynamic plasticity of heat-treated alloy (780 °C/1 h/AC) is lower than that of as-cast alloy due to the more TiC precipitates (see Fig. 7(c)).

#### 4. Conclusion

The main aim of this work is to determine the formation mechanism of trace TiC in an as-cast Ti13V11Cr3Al titanium alloy and understand the effects of this precipitate on the dynamic compressive properties of the alloy. The major conclusions of this work are summarized as follows:

- 1 A Ti13V11Cr3Al titanium alloy ingot with a small volume fraction of in-situ needle-like TiC precipitates is innovatively fabricated via vacuum induction skull melting.
- 2 The pseudo-phase equilibrium diagram for (Ti13V11Cr3Al)-C is constructed using CALPHAD model of JMatPro software. The calculation results indicate that precipitation of TiC will occur if the carbon content exceeds the critical carbon level (0.003 wt%). Furthermore, the Scheil-Gulliver simulations suggests that the maximum content of TiC precipitates is ~0.075 wt% during solidification of the Ti13V11Cr3Al titanium alloy.
- 3 The as-cast Ti13V11Cr3Al titanium alloy (compressive strength: 1350 MPa) is characterized by a critical fracture strain of >35% at a strain rate of 4158/s, thereby exhibiting excellent dynamic plasticity; the microstructural evolution of the ASB reveals that the TiC precipitates will be pulled out from the matrix (by overcoming the friction resistance) and, hence, considerable energy dissipation is required. Moreover, the crack path will deviate from the original direction and propagate along the boundary of these precipitates, thereby leading to significant improvement in the dynamic plasticity from the other respect.

#### Declaration of competing interest

The authors declare that they have no known competing financial interests or personal relationships that could have appeared to influence the work reported in this paper.

#### CRedit authorship contribution statement

**Duoduo Wang:** Data curation, Writing - original draft, Visualization. **Qunbo Fan:** Writing - review & editing, Resources, Supervision. **Hai-chao Gong:** Investigation. **Xinjie Zhu:** Investigation.

#### Acknowledgments

This work was supported by the National Natural Science Foundation of China (Grant No. 51571031).

#### References

- [1] E. Wielewski, G.J. Appleby-Thomas, P.J. Hazell, A. Hameed, An experimental investigation into the micro-mechanics of spall initiation and propagation in Ti-6Al-4V during shock loading, *Mater. Sci. Eng., A* 578 (20) (2013) 331–339.
- [2] K. Sun, X.D. Yu, C.W. Tan, H.L. Ma, F.C. Wang, Influence of adiabatic shear bands intersection on the ballistic impact of Ti-6Al-4V alloys with three microstructures, *Mater. Sci. Eng.* 606 (12) (2014) 257–267.
- [3] B. Bhav Singh, G. Sukumar, Amit Bhattacharjee, K. Siva Kumar, T. Balakrishna Bhat, A.K. Gogia, Effect of heat treatment on ballistic impact behavior of Ti-6Al-4V against 7.62 mm deformable projectile, *Mater. Des.* 36 (2012) 640–649.
- [4] Z. Tarzimoghadam, S. Sandlöbes, K.G. Pradeep, D. Raabe, Microstructure design and mechanical properties in a near- $\alpha$  Ti-4Mo alloy, *Acta Mater.* 97 (15) (2015) 291–304.
- [5] P.F. Gao, G. Qin, X.X. Wang, Y.X. Li, M. Zhan, G.J. Li, J.S. Li, Dependence of mechanical properties on the microstructural parameters of TA15 titanium alloy with tri-modal microstructure, *Mater. Sci. Eng., A* 739 (2) (2019) 203–213.
- [6] N. Wain, X.J. Hao, G.A. Ravi, X. Wu, The influence of carbon on precipitation of  $\alpha$  in Ti-5Al-5Mo-5V-3Cr, *Mater. Sci. Eng.* 527 (29–30) (2010) 7673–7683.
- [7] D.P. Zhao, T. Ebel, M. Yan, M. Qian, Trace carbon in biomedical beta-titanium alloys: recent progress, *J. Miner. Met. Mater. Soc.* 67 (10) (2015) 2236–2243.
- [8] D.P. Zhao, K.K. Chang, T. Ebel, M. Qian, R. Willumeit, M. Yan, F. Pyczak, Microstructure and mechanical behavior of metal injection molded Ti-Nb binary alloys as biomedical material, *J. Mech. Behav. Biomed. Mater.* 28 (2013) 171–182.
- [9] F. Kafkas, T. Ebel, Metallurgical and mechanical properties of Ti-24Nb-4Zr-8Sn alloy fabricated by metal injection molding, *J. Alloys Compd.* 617 (25) (2014) 359–366.
- [10] D.P. Zhao, K.K. Chang, T. Ebel, H. Nie, R. Willumeit, F. Pyczak, Sintering behavior and mechanical properties of a metal injection molded Ti-Nb binary alloy as biomaterial, *J. Alloys Compd.* 640 (15) (2015) 393–400.
- [11] M. Yan, M. Qian, C. Kong, M.S. Dargusch, Impacts of trace carbon on the microstructure of as-sintered biomedical Ti-15Mo alloy and reassessment of the maximum carbon limit, *Acta Biomater.* 10 (2) (2014) 1014–1023.
- [12] Z.X. Du, S.L. Xiao, P.X. Wang, L.J. Xu, Y.Y. Chen, H.K.S. Rahoma, Effects of trace TiB and TiC on microstructure and tensile properties of  $\beta$  titanium alloy, *Mater. Sci. Eng.* 596 (24) (2014) 71–79.
- [13] X.J. Zhang, F. Song, Z.P. Wei, W.C. Yang, Z.K. Dai, Microstructural and mechanical characterization of in-situ TiC/Ti titanium matrix composites fabricated by graphene/Ti sintering reaction, *Mater. Sci. Eng.* 705 (29) (2017) 153–159.
- [14] S.Y. Liu, Y.C. Shin, The influences of melting degree of TiC reinforcements on microstructure and mechanical properties of laser direct deposited Ti6Al4V-TiC composites, *Mater. Des.* 136 (15) (2017) 185–195.
- [15] K.S. Munir, Y.C. Li, J.X. Lin, C.E. Wen, Interdependencies between graphitization of carbon nanotubes and strengthening mechanisms in titanium matrix composites, *Materialia* 3 (2018) 1–17, 000.
- [16] L.J. Huang, L. Geng, H.Y. Xu, H.X. Peng, In situ TiC particles reinforced Ti6Al4V matrix composite with a network reinforcement architecture, *Mater. Sci. Eng.* 528 (6) (2011) 2859–2862.
- [17] Z. Liu, D.C. Zhang, L.J. Gong, J.G. Lin, C.E. Wen, Microstructures and mechanical properties of in situ TiC- $\beta$ -Ti-Nb composites with ultrafine grains fabricated by high-pressure sintering, *Sci. Rep.* 8 (2018) 9496.
- [18] S. Mereddy, M.J. Bermingham, D. Kent, A. Dehghan-Manshadi, D.H. Stjohn, M. S. Dargusch, Trace carbon addition to refine microstructure and enhance properties of additive-manufactured Ti-6Al-4V, *J. Miner. Met. Mater. Soc.* 70 (9) (2018) 1670–1676.
- [19] M. Chu, X.H. Wu, I.P. Jones, M.H. Loretto, Influence of carbon on aging response and tensile properties of eutectoid beta titanium alloy Ti-13Cr, *Mater. Sci. Technol.* 22 (6) (2006) 661–666.
- [20] M. Chu, I.P. Jones, X.H. Wu, Effect of carbon on microstructure and mechanical properties of a eutectoid  $\beta$  titanium alloy, *J. Mater. Eng. Perform.* 14 (2005) 735–740.
- [21] Y.G. Li, P.A. Blenkinsop, M.H. Loretto, D. Rugg, W. Voice, Effect of carbon and oxygen on microstructure and mechanical properties of Ti-25V-15Cr-2Al (wt%) alloys, *Acta Mater.* 47 (10) (1999) 2889–2905.
- [22] Y.J. Hao, J.X. Liu, J.C. Li, S.K. Li, Q.H. Zou, X.W. Chen, Rapid preparation of TiC reinforced Ti6Al4V based composites by carburizing method through spark plasma sintering technique, *Mater. Des.* 65 (2015) 94–97.
- [23] W.J. Lu, D. Zhang, X.N. Zhang, R.J. Wu, T. Sakata, H. Mori, Microstructural characterization of TiC in in situ synthesized titanium matrix composites prepared by common casting technique, *J. Alloys Compd.* 327 (1–2) (2001) 248–252.
- [24] X.X. Li, J.Y. Xiang, W.T. Hu, {111} twinning structure and interfacial energy in nonstoichiometric TiC<sub>x</sub> with ordered carbon vacancies, *Mater. Char.* 90 (2014) 94–98.
- [25] H.W. Xiong, Y. Guo, Z.Y. Li, K.C. Zhou, New production of (Ti, W)C-based cermets toughened by in-situ formed WC and twinned (Ti, W)C platelets: carbonization of the Nix(Ti<sub>0.6</sub>, W<sub>0.4</sub>)<sub>4</sub>C-type  $\eta$  phases, *J. Alloys Compd.* 731 (15) (2018) 253–263.
- [26] Z. Guo, N. Saunders, A.P. Miodownik, J.-Ph Schillé, Modelling of materials properties and behaviour critical to casting simulation, *Mater. Sci. Eng.* 413–414 (15) (2005) 465–469.
- [27] E. Abbasi, K. Dehghani, Phase prediction and microstructure of centrifugally cast non-equiatomic Co-Cr-Fe-Mn-Ni(Nb,C) high entropy alloys, *J. Alloys Compd.* 783 (30) (2019) 292–299.
- [28] S.Z. Zhang, M.M. Li, L.Q. Chen, Flow behavior and microstructure evolution during double-hit compression of Ti-5.6Al-4.8Sn-2Zr-1Mo-0.35Si-0.7Nd titanium alloy, *Mater. Sci. Eng.* 564 (1) (2013) 317–323.
- [29] J. Luo, L. Li, M.Q. Li, The flow behavior and processing maps during the isothermal compression of Ti17 alloy, *Mater. Sci. Eng.* 606 (12) (2014) 165–174.
- [30] J. Luo, J. Gao, L. Li, M.Q. Li, The flow behavior and the deformation mechanisms of Ti-6Al-2Zr-2Sn-2Mo-1.5Cr-2Nb alloy during isothermal compression, *J. Alloys Compd.* 667 (15) (2016) 44–52.
- [31] M. Hokka, T. Leemet, A. Shrot, M. Baeker, V.T. Kuokkala, Characterization and numerical modeling of high strain rate mechanical behavior of Ti-15-3 alloy for machining simulations, *Mater. Sci. Eng.* 550 (30) (2012) 350–357.

- [32] C. Ran, P.W. Chen, L. Li, W.F. Zhang, Y.L. Liu, X. Zhang, High-strain-rate plastic deformation and fracture behaviour of Ti-5Al-5Mo-5V-1Cr-1Fe titanium alloy at room temperature, *Mech. Mater.* 116 (2018) 3–10.
- [33] S. Sharma, A.N. Majilla, V.M. Chavan, D. Chandru Fernando, R.J. Patel, S.N. Babu, Deformation response of titanium alloy under static and dynamic loading, *Procedia Eng.* 173 (2017) 1894–1900.
- [34] Z.Z. Li, B.F. Wang, S.T. Zhao, R.Z. Valiev, K.S. Vecchio, M.A. Meyers, Dynamic deformation and failure of ultrafine-grained titanium, *Acta Mater.* 125 (15) (2017) 210–218.